Journal of Zhejiang University-SCIENCE A (Applied Physics & Engineering) in press
www.jzus.zju.edu.cn; www.springer.com/journal/11582
E-mail: jzus_a@zju.edu.cn

Research Article

https://doi.org/10.1631/jzus.A2400165

Cooperative optimization of the dynamic response and power losses of a water hydraulic high-speed on/off valve based on NSGA-II

Lingkang MENG[1], Defa WU[1]✉, Fengwei XU[2], Xing YANG[1], Zhengzheng ZHANG[2], Yinshui LIU[1]

[1]*School of Mechanical Science and Engineering, Huazhong University of Science and Technology, Wuhan 430074, China*
[2]*China Ship Scientific Research Center, Wuxi 214082, China*

Abstract: As vital indexes to evaluate the comprehensive performance of high-speed on/off valves (HSVs), the dynamic response and power losses are affected by the plus width modulation (PWM) control parameters. However, optimizing PWM control parameters to improve dynamic response and power losses simultaneously is challenging. This study focused on a water hydraulic HSV. Firstly, the effects of PWM control parameters on the dynamic response and power losses of the HSV were deeply analyzed using the finite element method. Then, Kriging models were constructed between opening time, closing time, total power loss, and the PWM control parameters of the HSV based on the optimal Latin hypercube sampling method and simulation results. On this basis, a multi-objective optimization method was used to find the optimal PWM control parameters. Finally, an experiment was performed to validate the simulation and optimization results. Results indicated that increasing the positive voltage amplitude and the duration of the negative voltage had a positive effect on reducing the total dynamic response time of the HSV, while increasing the duration of the positive voltage and the holding voltage amplitude had a negative effect. In addition, increasing all these PWM control parameters negatively affected the reduction of the total power loss of the HSV. Based on the optimized PWM control parameters, the experimental test times of the HSV on and off were 2.38 ms and 1.29 ms, respectively, and its steady-state temperature was 61.5 ℃, which met the requirements.

Key words: Cooperative optimization; Water hydraulic high-speed on/off valve; Dynamic response; Power losses; PWM control parameters

1 Introduction

With their urgent demand for resources, human beings have turned their attention from the land to the ocean. This has promoted the vigorous development of underwater equipment (He et al., 2023; Ge et al., 2024). Underwater hydraulic manipulators with a high power-to-weight ratio play a critical role in various underwater applications, such as resource exploration and underwater manipulation (Youakim et al., 2020; Shang et al., 2023).

Nowadays, as key control components, oil hydraulic proportional/electrohydraulic servo valves have been applied to control underwater hydraulic manipulators (Sarkar et al., 2023). However, with an increase in service time, the risk of oil-water mutual penetration of the oil hydraulic valves will increase, reducing the reliability of underwater hydraulic manipulators and adversely impacting the marine environment (Nieminen et al., 2009). Therefore, it is necessary to develop a water hydraulic valve (Siivonen et al., 2019). Due to the advantages of fast response, insensitivity to pollution, and good sealing, a high-speed on/off valve (HSV) using water as a working medium may be a good option (Nie et al., 2022).

HSV outputs the flow by switching on/off, but this also makes the output flow discrete, which is not beneficial to the precise control of the actuator (Zhong et al., 2022a). Enhancing the response frequency of the HSV is one of the best ways to compensate for this shortcoming, making dynamic response one of the key performance parameters to

✉ Defa WU, defawu@hust.edu.cn
Defa WU, https://orcid.org/0000-0002-0098-894X
Lingkang MENG, https://orcid.org/0000-0001-8300-4311

Received Mar. 23, 2024; Revision accepted July 20, 2024; Crosschecked

© Zhejiang University Press 2024

Unedited

judge the quality of the comprehensive characteristics of an HSV, whether water or oil hydraulic (Lantela and Pietola, 2017). Many scholars have focused on improving the dynamic response of HSVs. In structure, Wu et al. (2018) built a mathematical model of an HSV, and based on this model, a particle swarm optimization method was used to reduce its response times. Since the working process of an HSV involves multiple physical fields, its working characteristics are highly nonlinear (Taghizadeh et al., 2009). Therefore, establishing an accurate mathematical model of an HSV to describe its dynamic characteristics is difficult. The finite element method can accurately solve the electromagnetic characteristics of an HSV (Fan et al., 2023). However, achieving high simulation accuracy complicates the finite element simulation and increases time consumption, resulting in a low optimization efficiency of HSV performance. Numerous surrogate models, including the response surface model (RSM), Kriging model, and Radial base function (RBF) model, have been developed to improve optimization efficiency by establishing approximate mathematical models between the input variables and objective values based on a minimum of information (Yin et al., 2023). Some advanced optimization algorithms have also been created to optimize the surrogate models to obtain the Pareto solutions (Zhang et al., 2022). Li et al. (2021) constructed a second-order RSM between electromagnetic force, moving parts mass, and structural parameters of HSV and used a multi-objective optimization algorithm to obtain the best solution. Liu et al. (2021) established an RBF model between response times and structure parameters of HSV and used the non-dominated sorting genetic algorithm II (NSGA-II) and Technique for Order Preference by Similarity to Ideal Solution (TOPSIS) methods to determine the final solution.

Optimizing the driving strategy is a feasible approach to reduce the response times without changing the structure of existing HSVs. Instead of the traditional plus width modulation (PWM) control method, Zhou et al. (2016) adopted a new PWM control method with double voltages, in which the high voltage is used to shorten the HSV opening time, and the low voltage is used to reduce the closing time. Lee (2006) designed a driving circuit with three voltage sources, making the HSV close faster due to the negative high voltage. However, the durations of different driving voltages need to be debugged and set in advance. Therefore, the effects of the driving voltage durations on the response speed have been further studied (Yue et al., 2021). Without setting in advance, Zhang et al. (2018) put forward an intelligent driving strategy supported by current feedback to achieve automatic adjustment of driving voltages.

Although increasing the driving voltage can improve their dynamic performance, HSVs inevitably generate more power losses because the high voltages increase the amplitude and change rate of the coil current. Power losses can be converted into significant heat, resulting in a rise in the temperature of the HSV, degrading its dynamic performance and even causing it to fail (Liniger et al., 2020). Power losses also play a vital role in evaluating the overall performance of HSVs. Therefore, some scholars have further considered the power losses of HSVs while studying their dynamic performance. Cheng et al. (2015) investigated the effects of different control strategies on the dynamic performance and power losses of an HSV. For the single control parameters, increasing the firing current and driving voltage can reduce the opening time, but will lead to excessive power losses (Wang et al., 2016; Zhao et al., 2017a). In addition, Zhao et al. (2018b) found that reducing the holding current can shorten the closing time of HSV and reduce the power losses. The above research has shown that the control parameters significantly influence the comprehensive performance of HSVs.

Adopting a multi-voltage control strategy is necessary to improve the comprehensive performance of HSVs (Zhong et al., 2024b). To give full play to the advantages of a multi-voltage control strategy, the effects of the PWM control parameters, including the amplitude and duration of different driving voltages, need to be investigated in detail and optimized, which has rarely been reported. Therefore, in this study, we used a water hydraulic HSV as a research object. Firstly, the influence of the PWM control parameters on the dynamic response and power losses of the HSV were analyzed using finite element simulation. Then, the PWM control parameters were optimized based on optimal Latin hypercube sampling (OLHS), Kriging model, NSGA-II, and TOPSIS optimization

Unedited

algorithm frameworks to obtain the best solution. Finally, an experiment was conducted to verify the simulation and optimization results. This study provided an effective collaborative optimization method to improve the comprehensive performance of HSVs.

2 Structure and working principle

Fig. 1a shows a three-dimensional model of a water hydraulic HSV. It is a 2/2 and resting state closed HSV, consisting mainly of electromagnet and valve body assemblies. The electromagnet assembly includes mainly an iron core (1), coil (2), magnetic isolation ring (5), and armature (7). The valve body assembly comprises mainly a spring (3), spring seats (4), supporting ring (6), push rod (8), seal ball (9), and ball seat (10). The iron core and armature are made from 1J117 soft magnetic stainless steel materials. Other components of the HSV are made from 316L stainless steel materials, whose magnetic conductivity is very weak and almost the same as that of air.

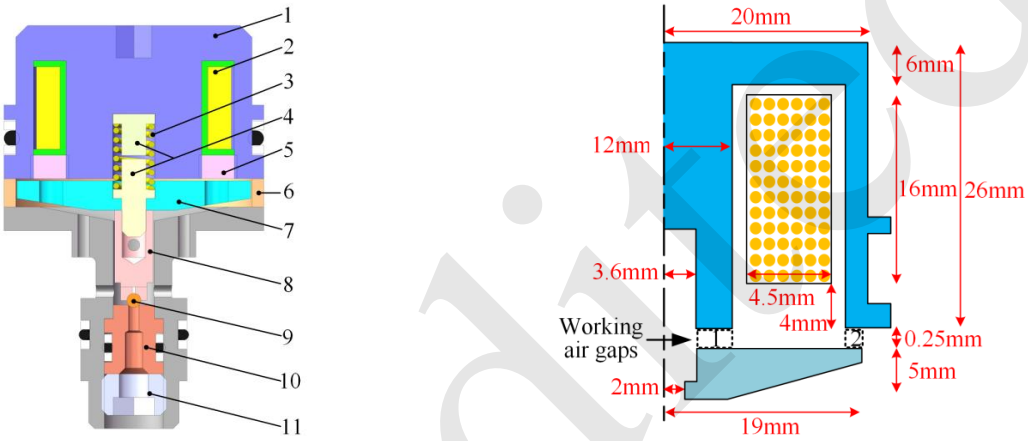

(a) (b)

1. Iron core; 2. Coil; 3. Spring; 4. Spring seats; 5. Magnetic isolation ring; 6. Supporting ring; 7. Armature; 8. Push rod; 9. Seal ball; 10. ball seat; 11. Locking screw.

Fig. 1 Schematic diagram of water hydraulic HSV: (a) Three-dimensional model; (b) Simplified geometry diagram

Initially, without external excitation, the HSV does not work. When the coil is excited by an external voltage, the armature will move upward under the combined electromagnetic force and spring force. Some key structural parameters of the HSV are presented in Fig. 1b. Table 1 lists other vital parameters.

Table 1 Structural parameters of the water hydraulic HSV.

Parameters	Value	Unit
Resistance of coil R	0.55	Ω
Turns of coil N	53	-
Pre-compression of spring l_0	3.5	mm
Stiffness of spring K_t	39	N mm^{-1}
Maximum displacement x_m	0.2	mm
Mass of moving parts m	0.048	kg

3 Mathematical models

3.1 Electromagnetic and mechanical models

The coil of an HSV can be regarded as an element with a resistor and an inductor in series. When an external voltage signal is input into the coil, the electrical model of the HSV is:

$$U = iR + i\frac{\mathrm{d}L}{\mathrm{d}t} + L\frac{\mathrm{d}i}{\mathrm{d}t}, \tag{1}$$

where U refers to the external excitation voltage, i is the excitation current, R represents the coil resistance, and L represents the coil inductance.

Due to the coil excitation, the magnetic circuit model of the HSV is as follows:

$$Ni = \phi R_m, \tag{2}$$

$$L = \frac{N^2}{R_m}, \tag{3}$$

where N denotes the coil turns, and ϕ and R_m are the magnetic flux and reluctance of the magnetic circuit, respectively.

Unedited

The electromagnetic force F_m on the armature can be calculated by:

$$F_m = \frac{\phi^2}{2\mu_0 A_s}, \tag{4}$$

where μ_0 refers to the air magnetic permeability, and A_s denotes the area of working air gaps.

In this study, the hydraulic characteristic was not considered. Moreover, the gravity of the movement components was neglected because of its small influence compared with other forces. The dynamic equation of the HSV can be written as:

$$m\frac{\mathrm{d}x^2}{\mathrm{d}t^2} = F_m - K_t\left(l_0 + x\right), \tag{5}$$

where m is the movement components mass, K_t is the spring stiffness, l_0 is the spring pre-compression, and x is the armature displacement.

Fig. 2 presents the complete dynamic response process of the HSV, which can be divided into six stages: the opening delay stage, opening moving stage, fully-open maintenance stage, closing delay stage, closing stage, and fully-close maintenance stage.

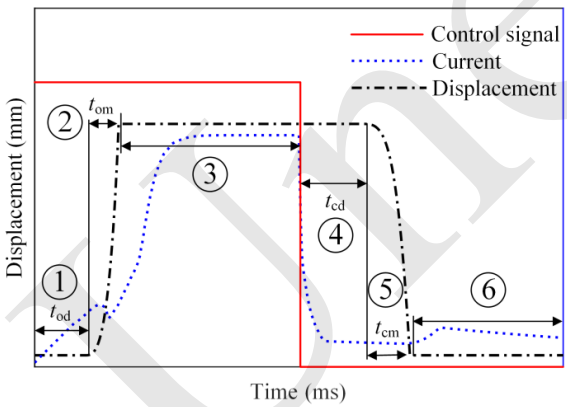

Fig. 2 Dynamic response process of the HSV.

Therefore, the opening and closing times t_o and t_c of the HSV can be written as:

$$t_o = t_{od} + t_{om}, \tag{6}$$

$$t_c = t_{cd} + t_{cm}, \tag{7}$$

where t_{od} and t_{om} represent the opening delay and opening moving times, respectively, and t_{cd} and t_{cm} denote the closing delay and closing moving times, respectively.

3.2 Power loss models

The energy conversion process of an HSV involves multiple physical fields, i.e., electric, magnetic, and mechanical. When an external voltage is input, the coil of the HSV is excited and generates a magnetic field, realizing the conversion of electrical energy into magnetic energy. Meanwhile, the moving parts begin to move under the attraction of electromagnetic force, which means that the magnetic energy is converted into mechanical energy. However, most energy in this conversion process is not fully used and is converted into harmful heat. Stranded loss, core loss, and solid loss are the three main manifestations of the power losses of an HSV.

In this study, we considered only the stranded loss of the HSV itself. Therefore, the stranded loss $P_{\text{strandedloss}}$ can be regarded as the resistive loss in the coil, which can be obtained by:

$$P_{\text{strandedloss}} = i^2 R, \tag{8}$$

Core loss is generated owing to the eddy current in the magnetic elements, which includes three main types: eddy current loss P_c, hysteresis loss P_h, and excess loss P_e. The core loss P_{coreloss} is obtained by:

$$P_{\text{coreloss}} = P_c + P_h + P_e, \tag{9}$$

$$P_c = k_c f^2 B_m^2, \tag{10}$$

$$P_h = k_h f B_m^2, \tag{11}$$

$$P_e = k_e f^{1.5} B_m^{1.5}, \tag{12}$$

where k_c, k_h, and k_e denote the coefficients of the eddy current, hysteresis, and excess losses, respectively, f refers to the magnetic field frequency, and B_m represents the magnetic induction intensity.

Due to the resistivity of magnetic elements, when the induced current passes through the magnetic elements, solid loss $P_{\text{solidloss}}$ is produced, which can be written as:

$$P_{\text{solidloss}} = \int_V \frac{J^2 dV}{\sigma}, \tag{13}$$

where J is the induced current density, σ denotes the conductivity of magnetic elements, and V represents

Unedited

the volume of magnetic elements.

Therefore, the total power loss P_t of the HSV can be expressed as:

$$P_t = P_{\text{strandedloss}} + P_{\text{coreloss}} + P_{\text{solidloss}}. \tag{14}$$

4 Numerical simulation method

4.1 Simulation model and settings

Considering that the energy conversion during the transient motion of the HSV is very complex, the finite element method was used to analyze dynamic response and power losses during the HSV action. Fig. 3a shows the finite element model of the HSV. Only the magnetic components of the HSV, including iron, coil, and armature were considered, to save calculation time. The model also includes the calculation and motion domains, i.e., the region and band. Fig. 3b shows all the calculation domains meshed by the adaptive mesh refinement method with unstructured tetrahedral mesh (Wang, et al., 2016). The *B-H* magnetization curve of the 1J117 soft magnetic material is presented in Fig. S1 of the electronic supplementary materials (ESM). The detailed settings of the simulation parameters and methods are presented in Table S1 of the ESM.

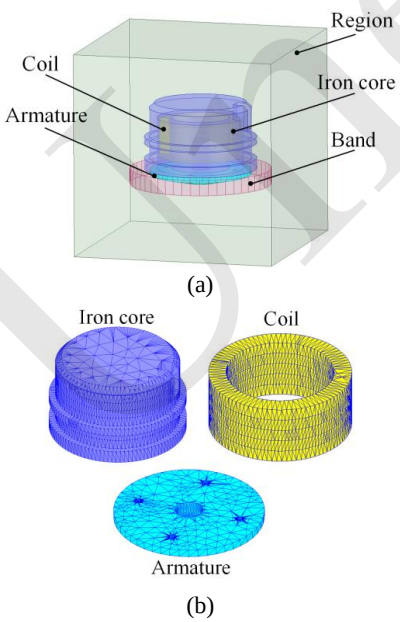

Fig. 3 Finite element and meshing models of the HSV: (a) Finite element model; (b) Meshing model

4.2 Control strategy

Fig. 4 shows a compound PWM (CPWM) driving method, consisting of multiple PWM voltage signals, including positive, high-frequency holding, and negative voltages.

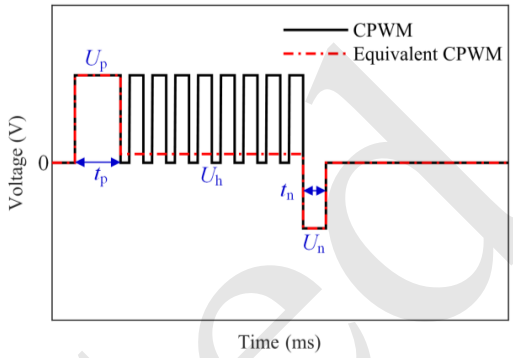

Fig. 4 CPWM control strategy of the HSV.

The positive voltage amplitude and the negative voltage amplitude are determined by DC power, while the equivalent amplitude of high-frequency holding voltage can be calculated by:

$$U_h = U\tau_h, \tag{15}$$

where U_h and τ_h are the equivalent amplitude and duty ratio of the high-frequency holding voltage, respectively.

The quality of the CPWM control strategy is determined by the PWM control parameters, including the amplitude of the positive voltage U_p, the duration of the positive voltage t_p, the equivalent amplitude of the high-frequency holding voltage U_h, the amplitude of the negative voltage U_n ($U_n = -U_p$), and the duration of the negative voltage t_n. Only by selecting the appropriate PWM control parameters can we fully exploit the advantages of the CPWM control strategy, thereby speeding up the dynamic response of the HSV and saving its energy consumption.

4.3 Validation of simulation model

Fig. 5 presents a test rig used to verify the simulation model of the HSV. This test rig tests the coil current and opening and closing times of the HSV. DC power is supplied to the driver. The function of the host computer is to send excitation signals to the driver. The driver is used to amplify the power of the excitation signal. The current sensor (Shenzhen

Unedited

Zhiyong Co., Ltd, HCP8050) is used to detect the coil current. The laser displacement sensor (KEYENCE Co., Ltd, LK-G5000) is used to obtain the armature displacement. Owing to the structure of the HSV, it is difficult to measure the displacement of the armature directly. Therefore, a designed resin sheet with a small mass was stuck on the side of the armature. When the spot emitted by the laser displacement sensor is irradiated on the resin sheet, the armature displacement can be measured in real time. The oscilloscope was applied to collect the coil current and armature displacement signals, which needed to be post-processed to obtain actual values.

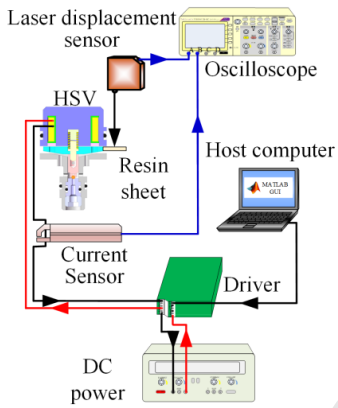

(a)

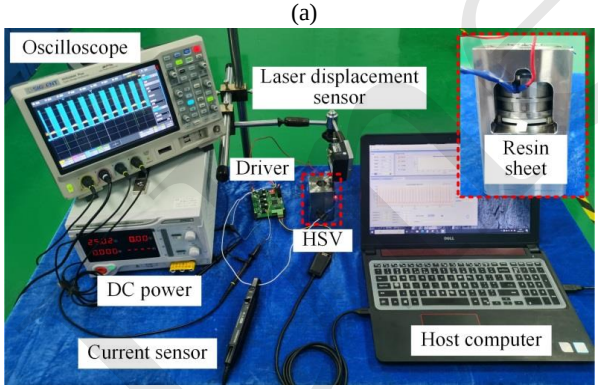

(b)

Fig. 5 Test bench for the performance of the HSV: (a) Schematic diagram of test bench; (b) Physical diagram of test bench

Operation of the HSV incurs many kinds of power losses which are difficult to measure accurately by experiment. According to the above analysis, the current determines the stranded loss, and the current change rate directly influences the core loss and solid loss. It can be considered that the current alone almost determines the power losses of the HSV. Therefore, the simulated power losses can be verified by comparing the coil current obtained from simulation and experiment. Under a typical excitation signal with a complete cycle (T=50 ms) and a duty cycle of 50 %, the coil current and armature displacement results of the simulation and experiment are shown in Fig. 6.

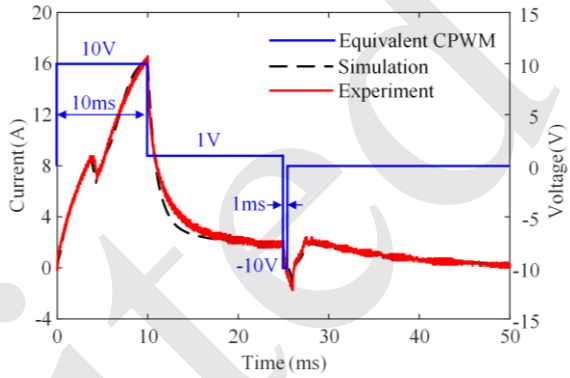

(a)

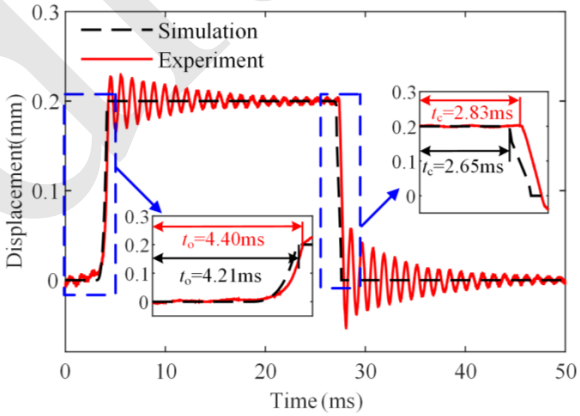

(b)

Fig. 6 Coil current and armature displacement from simulation and experiment for the HSV: (a) Current of coil; (b) Displacement of armature

Fig. 6a and 6b show that the coil current and the armature displacement of the simulation results are in good agreement with the experimental results. To visually show the comparison results, the opening and closing times of the HSV were selected as comparison values. Specifically, the opening times of the simulation and experiment were 4.21 ms and 4.4 ms, respectively, and their closing times were 2.65 ms and 2.83 ms, respectively. The errors between them were 0.19 ms (4.3 %) and 0.18 ms (6.4 %). The simulation results were always slightly smaller than the experimental results, due mainly to neglecting the

Unedited

mechanical friction of the moving components in the simulation model.

Moreover, in the experimental results of armature displacement, the armature will collide violently with other components under electromagnetic and spring forces when it reaches the upper and lower ends. Since the resin sheet stuck on the armature side has a slight stiffness, the resin sheet inevitably fluctuates owing to the impact. However, this did not affect the measurement of the response times. Generally, the simulation results of the HSV were very close to the experimental results. Therefore, we considered that the finite element simulation model of the HSV was reasonable and could be used for further analysis.

4.4 Simulation results analysis

4.4.1 Effects of positive voltage amplitude

Fig. 7 shows the effects of the positive voltage Up on the dynamic response and power losses of the HSV. Fig. 7a presents the coil current of the HSV with different U_p.

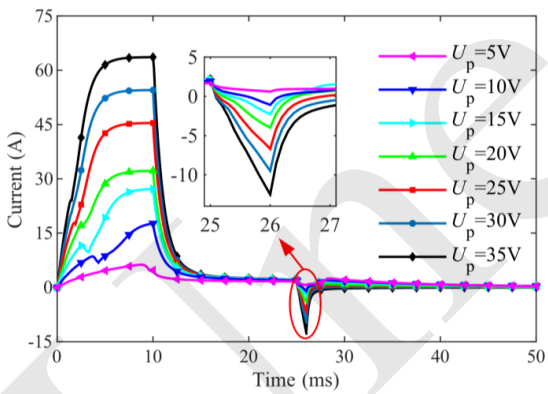

(a)

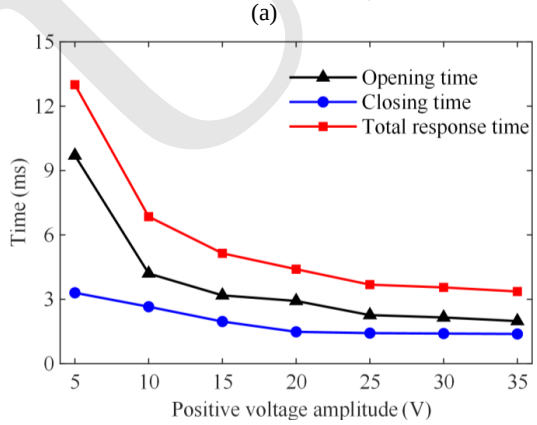

(b)

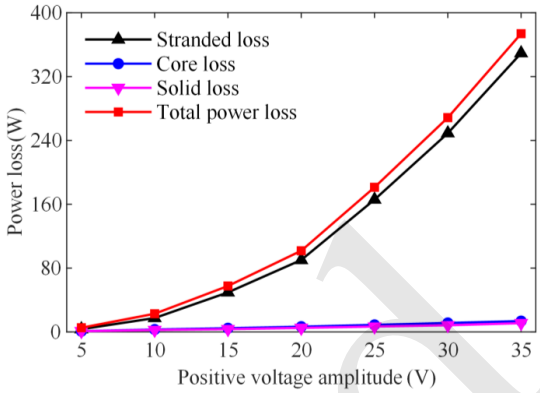

(c)

Fig. 7 Comparison of response times and power losses of the HSV under different U_p: (a) Coil current; (b) Response times; (c) Power losses

In Fig. 7b, as the U_p increases, the opening and closing times decrease, reducing the total response time. When the U_p increases from 5 to 35 V, the total response time decreases from 14.36 to 3.21 ms, a reduction of 77.6 %. This is because, with increasing U_p, the rising and falling rates of the coil current become faster in the opening process of the HSV. However, note that when the U_p increases to a certain extent beyond 25 V, the response times are little affected by the U_p.

With increasing U_p, the amplitude and change rate of the coil current increase rapidly (Fig. 7a), which inevitably increases the power losses of the HSV. Fig. 7c shows that the stranded, core, and solid losses all increase with increasing U_p. When the U_p changes from 5 to 35 V, they increase from 3.4 W, 0.91 W, and 0.86 W to 349.3 W, 13.5 W, and 10.9 W, respectively, and thus the total power loss increases significantly from 5.2 to 373.8 W, a 70.9-fold increase. The stranded loss is the largest, followed by the core loss and solid loss. When the U_p reaches 35 V, the stranded loss reaches a maximum of 93.5%, while the core loss and solid loss are only 3.6% and 2.9%, respectively. The power losses, especially stranded loss, can be converted into significant heat, causing the coil temperature to rise and degenerating the performance of the HSV.

The above analysis shows that the U_p has positive and negative effects on reducing the response times and power losses of the HSV, respectively. A higher U_p can reduce the response times but will increase the power losses, especially the stranded loss.

Unedited

4.4.2 Effects of positive voltage duration

Fig. 8 shows the effects of the positive voltage duration t_p on the dynamic response and power losses of the HSV. Fig. 8a presents the coil current of the HSV with different t_p.

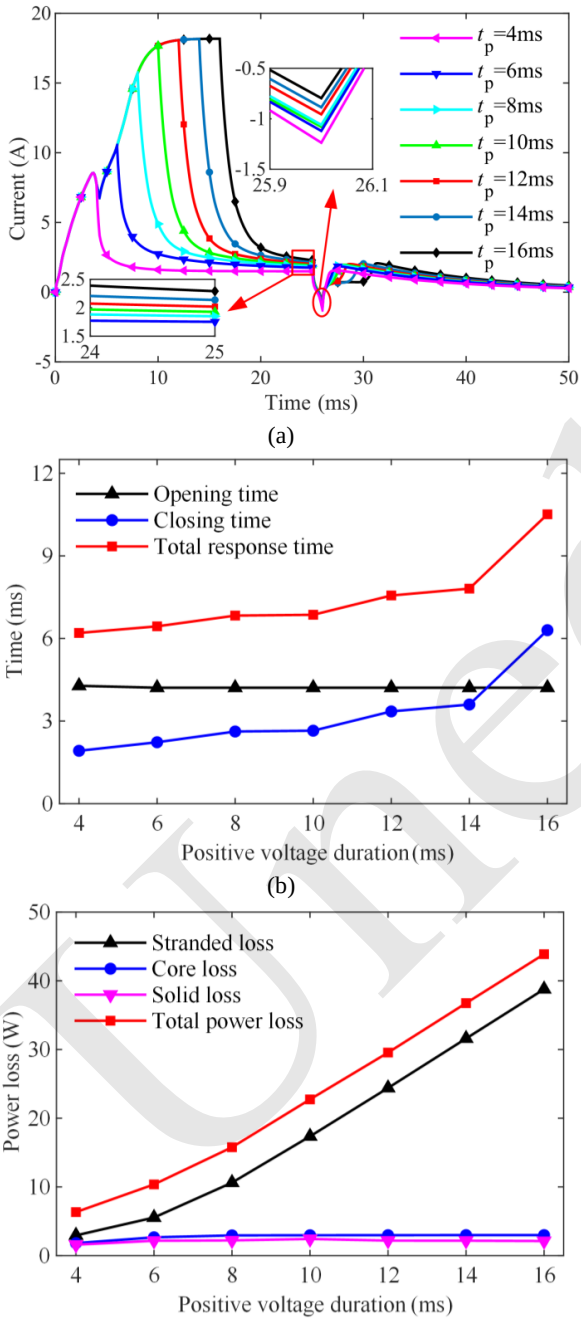

Fig. 8 Comparison of response times and power losses of the HSV under different t_p: (a) Coil current; (b) Response times; (c) Power losses

In Fig. 8b, when the t_p increases, the opening time of the HSV remains constant while the closing time decreases. When the t_p ranges from 4 to 16 ms, the opening time is always 4.21 ms, while the closing time increases from 1.92 to 6.3 ms. Thus, the total response time is extended from 6.2 to 10.51 ms, an increase of 69.5%. The main reason is that the coil current decreases slowly when the HSV receives a closing signal (Fig. 8a).

The longer t_p means more stranded loss due to the high current in the coil. Fig. 8c shows that with increasing t_p, the stranded loss increases, while the core increases slightly and the solid losses remain almost unchanged. When the t_p changes from 4 to 16 ms, the stranded loss increases from 2.9 to 38.8 W, a 12.4-fold increase. When the t_p increases from 4 to 6 ms, the core loss increases from 1.8 to 2.8 W and the solid loss from and 1.5 to 2.1 W, while as the t_p continues to increase, they remain almost constant. Thus, the total power losses increase from 6.2 to 44.4 W, a 6.2-fold increase.

The above analysis indicates that the t_p negatively affects the closing characteristic and stranded loss of the HSV while having little influence on the opening characteristic, core loss, and solid loss. A shorter t_p means a shorter closing time and less stranded loss. However, the t_p should be selected near the opening time of the HSV, otherwise it may not open entirely.

4.4.3 Effects of holding voltage amplitude

Fig. 9 shows the impacts of the high-frequency holding voltage U_h on the dynamic response and power losses of the HSV. Fig. 9a shows the coil current of the HSV with different U_h.

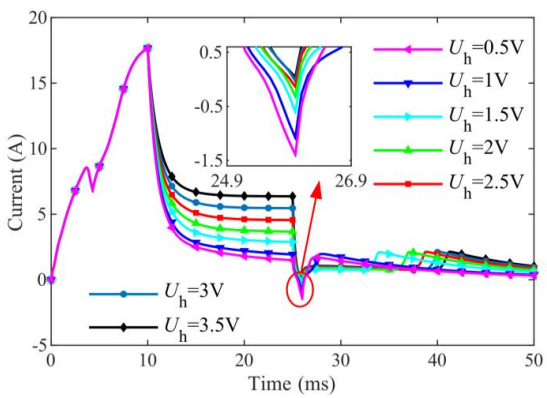

(a)

Unedited

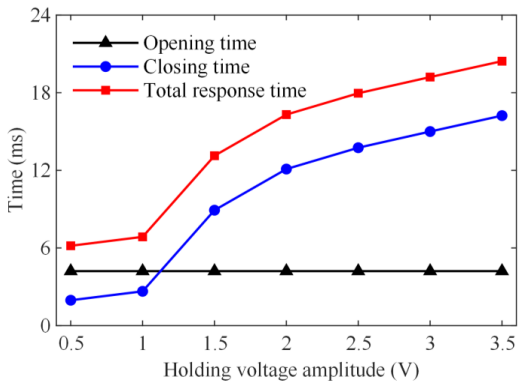

(b)

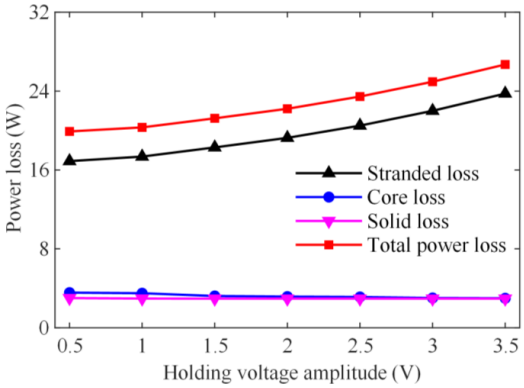

(c)

Fig. 9 Comparison of response times and power losses of the HSV under different U_h: (a) Coil current; (b) Response times; (c) Power losses

In Fig. 9b, when the U_h increases, the opening time remains unchanged while the closing time decreases. When the U_h increases from 0.5 to 3.5 V, the opening time remains at 4.21 ms, while the closing time increases from 1.96 to 16.2 ms, which indicates that the total response time increases significantly from 6.17 to 20.41 ms, a 2.3-fold increase. The main reason is that the increase in coil holding current leads to a slower decrease in current when the HSV is about to close.

The coil holding current increases with increasing U_h, which will inevitably increase the stranded loss. Fig. 9c shows that when the U_h increases, the stranded loss increases, while the core and solid losses decrease. When the U_h changes from 0.5 to 3.5 V, the stranded loss increases from 16.9 to 23.8 W, an increase of 40.8%. The core and solid losses decrease from 3.6 W and 3.1 W to 2.9 W and 2.8 W, respectively, reduced by 19.4% and 9.6%. As a result, the total power loss increases from 23.6 to 29.5 W, an increase of 25%.

According to the above analysis, the U_h has a negative effect on the closing characteristic and power losses of the HSV while having little effect on the opening characteristic. A smaller U_h means a shorter closing time and less power losses. However, U_h must be able to keep the HSV fully open.

4.4.4 Effects of negative voltage duration

Fig. 10 shows the effects of the negative voltage duration t_n on the dynamic response and power losses of the HSV. Fig. 10a shows the coil current of the HSV with different t_n.

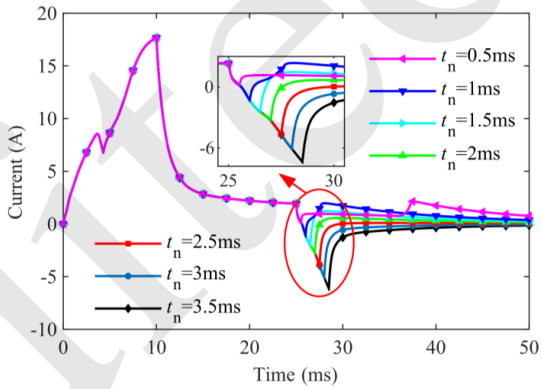

(a)

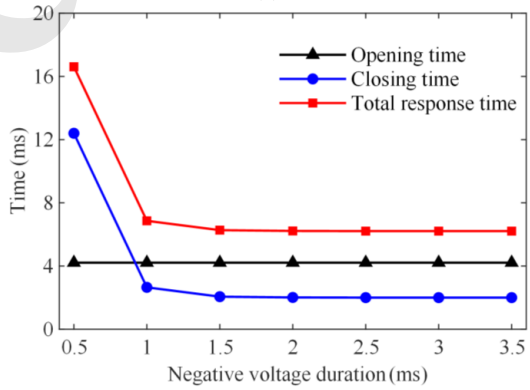

(b)

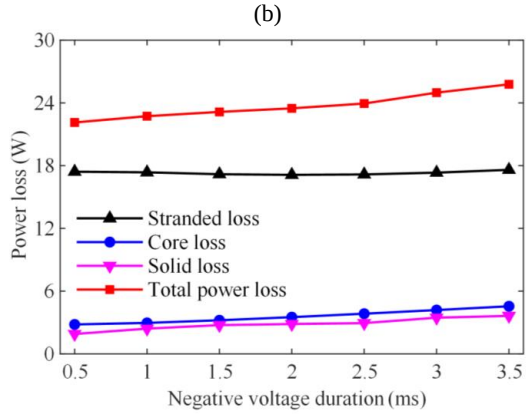

(c)

Unedited

Fig. 10 Comparison of response times and power losses of the HSV under different t_n: (a) Coil current; (b) Response times; (c) Power losses

In Fig. 10b, as the t_n increases, the opening time remains invariable, while the closing time decreases and then remains unchanged. When the t_n ranges from 0.5 to 3.5 ms, the opening time is always 4.21 ms. For the closing characteristic of the HSV, when the t_n changes from 0.5 to 1.5 ms, the closing time reduces from 12.4 to 2 ms. After that, the closing time remains unchanged, which is because the longer the t_n, the greater the amplitude of the current drop. However, when the t_n exceeds the closing time of the HSV, its closing behavior is not affected, no matter how much the current drops (Fig. 10a).

Unlike the effect of previous PWM control parameters (Fig. 10c), with increasing t_n, the stranded loss remains almost constant, while the core and solid losses increase. When the t_n changes from 0.5 to 3.5 ms, the stranded loss stays at around 17.4 W, while the core loss increases from 2.8 to 4.6 W and the solid loss from 1.9 to 3.6 W, due to a significant current drop. The total power loss increases from 22.1 to 25.6 W, an increase of 15.8%.

For the above analysis, we consider that the t_n positively affects the closing characteristic of the HSV when the t_n is less than the closing time of the HSV; otherwise, it does not. Note that the t_n cannot be increased too much, or it may cause the reverse current of the coil to be too large and destroy the working mechanism of the HSV. The t_n has a negative effect on the core and solid losses of the HSV, while having a minor influence on the stranded loss.

5 Multi-objective optimization method

5.1 Optimization problem statement

The above analysis (section 4.4) shows that the PWM control parameters significantly influence the dynamic response and power losses of the HSV, and the effects of each parameter differ. Therefore, it is necessary to optimize the PWM control parameters. We chose 4 PWM control parameters, including the positive voltage U_p, the positive voltage duration t_p, the equivalent amplitude of the high-frequency holding voltage U_h, and the negative voltage duration t_n, as design variables. The opening time t_o, closing time t_c, and total power loss P_t of the HSV were defined as objective functions. Fig. S2 of the ESM shows the multi-objective optimization process.

5.2 Design of experiments

Table 2 lists the value range of the design variables. Choosing suitable sample points from design variables is very important to ensure the accuracy of the surrogate model. This means that not only does there need to be a sufficient number of selected sample points but they also need to have typical representativeness. However, too many sample points will inevitably lead to high computational costs. To balance the representativeness and computational cost, the OLHS method was used to evenly distribute the sample points (Ghorani et al., 2020). Based on the OLHS method, 60 samples were generated.

Table 2 Range of design variables

Design variables	Minimum values	Maximum values
U_p(V)	5	35
t_p(ms)	1.5	10.5
U_h(V)	0.5	3.5
t_n(ms)	0.5	3.5

5.3 Surrogate model

Using a surrogate model instead of finite element simulation can save computing time and cost. Nevertheless, the surrogate model must be sufficiently accurate. Considering that there is a nonlinear relationship between design variables and objective functions, the Kriging model was used to build the approximate mathematical models because it has the advantage of fitting various nonlinear functions accurately (Chen et al., 2022). The primary expression is:

$$y(x) = \beta + z(x), \tag{16}$$

where β is the unknown constant of the regressed global trend model, and $z(x)$ represents localized deviations.

The finite element simulation solved the simulation results of the above 60 samples. Fifty design variables and their corresponding simulation results were selected to build the Kriging model, and the rest were used to verify the Kriging model by calculating the coefficient of determination R^2, the maximum absolute error (MAE), and the root mean square error (RMSE). The closer R^2 is to 1, and MAE and RMSE

Unedited

are to 0, the higher the accuracy of the Kriging model. Table 3 shows the test results of the Kriging models. The high R^2 and low MAE and RMSE values indicate their good prediction performance.

Table 3 Test results of Kriging models.

	R^2	MAE	RMSE
t_o	0.963	0.111	0.052
t_c	0.971	0.098	0.041
P_t	0.951	0.124	0.063

5.4 Multi-objective optimization method

This study had three optimization objectives, and the optimization mathematical model was:

$$\begin{cases} \text{Find}: \mathbf{x} = [U_p, t_p, U_h, t_n]^T \\ \text{Minimize}: \{t_o, t_c, P_t\} \\ \text{S.T}: \quad 5\text{V} \le U_p \le 35\text{V} \\ \qquad 1.5\text{ms} \le t_p \le 3.5\text{ms} \\ \qquad 0.5\text{V} \le U_h \le 3.5\text{V} \\ \qquad 0.5\text{ms} \le t_n \le 3.5\text{ms} \end{cases}, \tag{17}$$

The NSGA-II has good search performance and is suitable for contradictory and extensive targets, and has been verified to be a practical method for solving the multi-objective optimization problem (Shi et al., 2021). Therefore, we adopted the NSGA-II method to optimize. In this study, the main setting parameters of the NSGA-II were as follows: (1) Initial population size: 100; (2) Number of generations: 100; (3) Cross probability: 0.9; (4) Crossover distribution index: 10; (5) Mutation distribution index: 20.

5.5 Decision method

In this study, there was a contradiction in the optimization objective, i.e., the optimal solution of one objective function may not satisfy another. The TOPSIS method is widely used as a decision-making method to help designers choose the best compromise for multi-objective optimization problems (Ghasemi et al., 2016). By identifying the positive and negative ideal solutions, TOPSIS ranks each solution according to the Euclidian distance from the positive and negative ideal solutions (Allouhi et al., 2022). As a result, the relative closeness of each solution to the positive and negative ideal solutions can be obtained. The detailed steps for using this method are given in Section S1 of the ESM.

6 Optimization results and discussion

6.1 Optimization results and validation

By optimization, 472 Pareto optimal solutions were obtained (Fig. 11). Fig. 11a indicates that the relationship between the opening time and closing time is positive, which means they can be reduced simultaneously. In Fig. 11b and c, the opening and closing times conflict with the total power loss, indicating that minimizing those cannot be obtained simultaneously. Therefore, the designer needs to propose a compromise scheme. In this study, the dynamic response times of the HSV were considered equally important as power losses, so the weight of the objective functions, i.e., opening time, closing time, and total power loss, were set to be the same. The best compromise solution, based on the TOPSIS method, is shown in Fig. 11d.

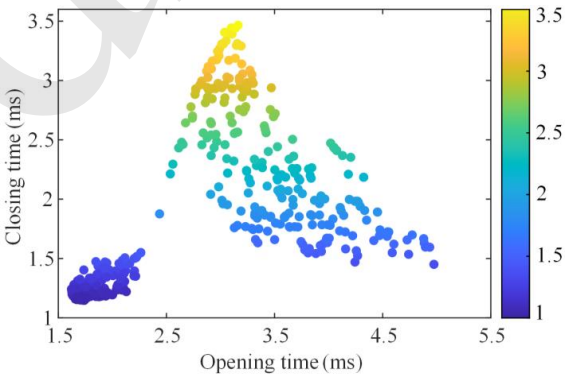

(a)

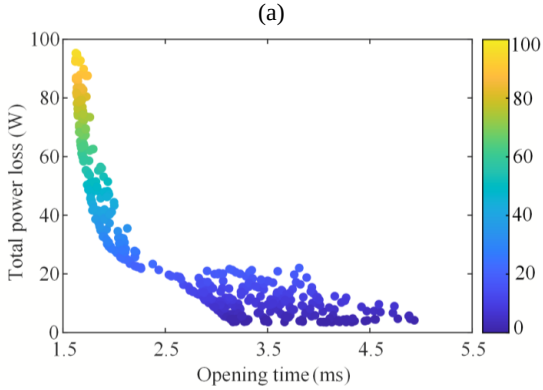

(b)

Unedited

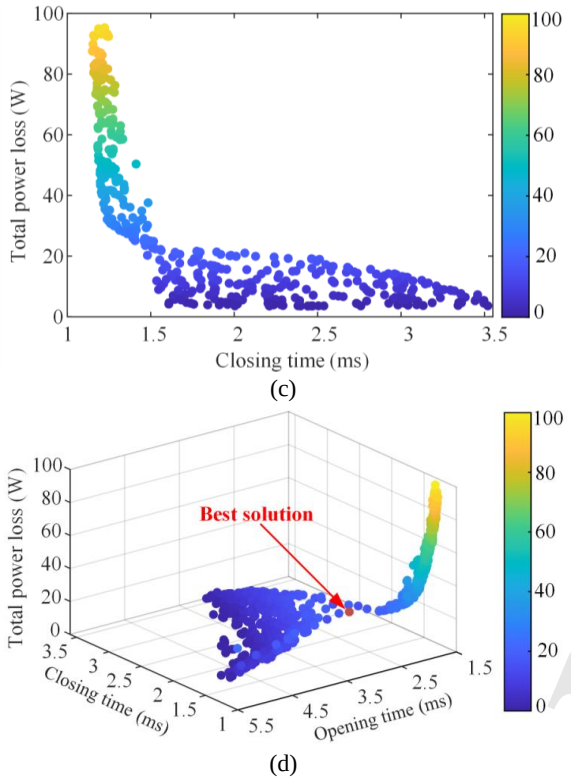

Fig. 11 Pareto optimal solutions of multi-objective optimization: (a) t_o & t_c; (b) t_o & P_t; (c) t_c & P_t; (d) t_o & t_c & P_t

Table 4 lists the final best solution and the corresponding PWM control parameters. The finite element simulation results are also compared with the best solution. Moreover, considering the actual operation of the driver, the PWM parameters are rounded. The opening time t_o and closing time t_c of the HSV obtained by the experiment are also presented in Table 4. The errors of the opening time, closing time, and total power loss between the optimization and simulation results were 3.5%, 5.9%, and 7.1%, respectively. Even after rounding, the experimental data agree well with the optimization results, and the maximum error was only 8.5%. The above comparison analysis indicates that the optimization results are valid.

Table 4 Results of the best compromise solution

Parameters	Optimal solution	Simulation validation	Experimental results
U_p(V)	24.82	24.82	25
t_p(ms)	2.48	2.48	2.5
U_h(V)	0.53	0.53	0.5
t_n(ms)	1.13	1.13	1.1
t_o(ms)	2.18	2.26	2.38
t_c(ms)	1.25	1.18	1.29
P_t(W)	24.85	23.2	-

Based on the rounded PWM control parameters, the power losses of the HSV were obtained by finite element simulation (Fig. 12). The changing trend of the stranded loss is the same as that of current amplitude, i.e., the larger the current amplitude, the larger the stranded loss. The core and solid losses occur mainly in the current change period, and increase with increasing current change rate. Among the above three power losses, the stranded loss accounted for the largest proportion (41.9%), followed by the core loss (30.7%) and the solid loss (27.4%).

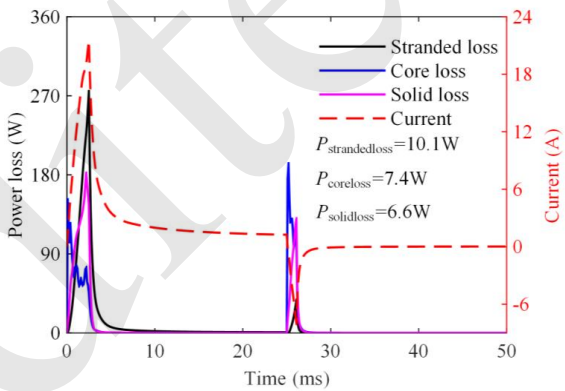

Fig. 12 Simulation results of power losses of HSV after optimization.

The temperature curve of the HSV with time was also tested using an infrared thermometer (Fig. 13). As time increased, the temperature of the HSV first increased and then stabilized, and 60 min was the critical point. After the running time exceeded 60 min, the temperature of the HSV remained almost unchanged at around 61.5 ℃.

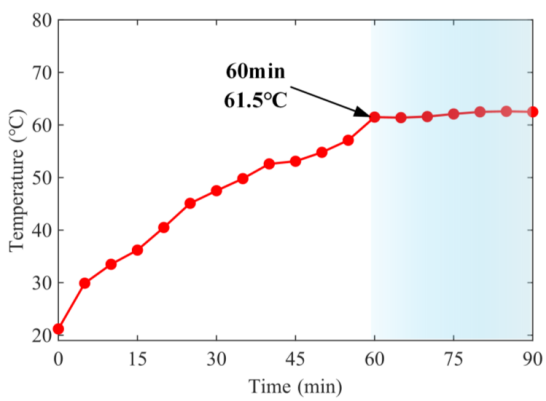

Unedited

Fig. 13 Temperature curve of HSV after optimization.

6.2 Discussion

According to the previous analysis, the PWM control parameters significantly affect the dynamic response times and power losses of an HSV. In addition, the method proposed in this study can effectively realize the cooperative optimization of the HSV for a fast dynamic response and low power losses.

Without depending on the precise mathematical model, the current-based feedback mechanism, and spending much time debugging PWM control parameters, this study achieved the optimal balance between the dynamic response and power losses of the HSV by optimizing a set of control parameters based on NSGA-II, supported by a Kriging model. This optimization method reduces the design difficulty of the hardware and software of the driver and simplifies the debugging process of the control parameters of the HSV in the early stage.

Given the application of the HSV in this study, we chose a compromise scheme to consider the short response times as well as the low power losses of the HSV simultaneously. However, we could choose other appropriate PWM control parameters for different working conditions by changing the weight of objective functions in the proposed combinatorial optimization algorithm. For example, in the hope that the HSV can move faster, the weight of the dynamic response can be appropriately increased, while that of the total power loss can be appropriately decreased, and vice versa. The proposed optimization method can help users determine the appropriate control parameters of HSVs to adjust their performance and adapt to different working conditions, which is conducive to promoting HSVs in the industrial field.

7 Conclusions

Based on a water hydraulic HSV, the effects of PWM control parameters on the dynamic response and the power losses of the HSV were studied. Furthermore, the optimization algorithm framework, composed of the OLHS, Kriging model, NSGA-II, and TOPSIS, was used to optimize the PWM control parameters to improve the comprehensive performance of the HSV. Our main conclusions are summarized as follows:

1. The PWM control parameters have a significant effect on the dynamic performance of an HSV. The higher the positive voltage amplitude, the shorter the opening time; the longer the negative voltage duration, the shorter the closing time; the longer the positive voltage duration and the larger the high-frequency holding voltage amplitude, the longer the closing time of the HSV.

2. The PWM control parameters significantly affect the power losses of an HSV. As positive voltage amplitude, positive voltage duration, high-frequency holding voltage amplitude, and negative voltage duration increase, the power losses of an HSV will increase.

3. The experimental and simulation data verified the optimization results, indicating that the proposed optimization method can improve the comprehensive performance of an HSV. The maximum deviation between the experimental and optimization results was 8.5 %. After optimization, the experimental results showed that the opening and closing times of the HSV were 2.38 ms and 1.29 ms, respectively, and its steady-state temperature was about 61.5 ℃.

Acknowledgments

We thank the National Natural Science Foundation of China (52122502), the National Key Research & Development Program of China (2022YFC2805705), the Fundamental Research Funds for the Central Universities (YCJJ20230358), and the Key Technology Tackling Project of Cold Spring Device of Chinese Academy of Sciences (LQ-GJ-01) for providing the funding for this research.

Author contributions

Lingkang MENG designed the research and wrote the first draft of the manuscript. Defa WU revised and edited the final version. Fengwei XU and Zhengzheng ZHANG processed the corresponding data. Xing YANG helped to organize the manuscript. Yinshui LIU revised the final version.

Conflict of interest

Lingkang MENG, Defa WU, Fengwei XU, Xing YANG, Zhengzheng ZHANG, and Yinshui LIU declare that they have no conflict of interest.

References

Allouhi H, Allouhi A, Jamil A, 2022. Multi-objective optimization of a csp-based dish stirling field layout using genetic algorithm and topsis method: Case studies in

Unedited

ouarzazate and madrid. *Energy Conversion and Management*, 254:115220. https://doi.org/10.1016/j.enconman.2022.115220

Chen L, Bao AM, Zhang Y, et al., 2022. Surrogate-based optimization and experiment validation of a fan-shaped film cooling hole with a large lateral space. *Applied Thermal Engineering*, 207:118145. https://doi.org/10.1016/j.applthermaleng.2022.118145

Cheng Q, Zhang ZD, Xie NL, 2015. Power losses and dynamic response analysis of ultra-high speed solenoid injector within different driven strategies. *Applied Thermal Engineering*, 91(0):611-621. https://doi.org/10.1016/j.applthermaleng.2015.08.053

Fan Y, Wang HA, Xie LT, et al., 2023. Armature structure optimization of annular multipole solenoid valves based on electromagnetic force distribution. *Actuators*, 12(2):54. https://doi.org/10.3390/act12020054

Ge D, Wang G, Ge J, et al., 2024. Trajectory tracking control of two-joint underwater manipulator in ocean-wave environment. *Ocean Engineering*, 292:116329. https://doi.org/10.1016/j.oceaneng.2023.116329

Ghasemi A, Gheydi M, Golkar MJ, Eslami M, 2016. Modeling of wind/environment/economic dispatch in power system and solving via an online learning meta-heuristic method. *Applied Soft Computing*, 43:454-468. https://doi.org/10.1016/j.asoc.2016.02.046

Ghorani MM, Haghighi MHS, Riasi A, 2020. Entropy generation minimization of a pump running in reverse mode based on surrogate models and nsga-ii. *International Communications in Heat and Mass Transfer*, 118 https://doi.org/10.1016/j.icheatmasstransfer.2020.104898

He F, Liu YB, Pan JP, et al., 2023. Advanced ocean wave energy harvesting: Current progress and future trends. *Journal of Zhejiang University-SCIENCE A*, 24(2):91-108. https://doi.org/10.1631/jzus.A2200598

Lantela T, Pietola M, 2017. High-flow rate miniature digital valve system. *International Journal of Fluid Power*, 18(3):188-195.

Lee IY, 2006. Switching response improvement of a high speed on/off solenoid valve by using a 3 power source type valve driving circuit. *2006 IEEE International Conference on Industrial Technology*, :1823-1828.

Li T, Zhang YT, Liang YX, et al., 2021. Multiobjective optimization research on the response time of a pneumatic pilot-operated high speed on/off valve. *International Journal of Applied Electromagnetics and Mechanics*, 65(1):109-127. https://doi.org/10.3233/Jae-190074

Liniger J, Stubkier S, Soltani M, Pedersen HC, 2020. Early detection of coil failure in solenoid valves. *IEEE/ASME Transactions on Mechatronics*, 25(2):683-693. https://doi.org/10.1109/Tmech.2020.2970231

Liu QT, Yin FL, Nie SL, et al., 2021. Multi-objective optimization of high-speed on-off valve based on surrogate model for water hydraulic manipulators. *Fusion Engineering and Design*, 173:112949. https://doi.org/10.1016/j.fusengdes.2021.112949

Nie SL, Liu QT, Ji H, et al., 2022. Integration of arima and lstm models forremaining useful life prediction of a water hydraulic high-speed on/off valve. *Applied Sciences*, 12(8071):8071. https://doi.org/10.3390/app12168071

Nieminen P, Esque S, Muhammad A, et al., 2009. Water hydraulic manipulator for fail safe and fault tolerant remote handling operations at iter. *Fusion Engineering and Design*, 84(7-11):1420-1424. https://doi.org/10.1016/j.fusengdes.2008.12.002

Sarkar A, Maji K, Chaudhuri S, et al., 2023. Actuation of an electrohydraulic manipulator with a novel feedforward compensation scheme and pid feedback in servo-proportional valves. *Control Engineering Practice*, 135:105490. https://doi.org/10.1016/j.conengprac.2023.105490

Shang DY, Li XP, Yin M, Li FJ, 2023. Vibration suppression method for flexible link underwater manipulator considering torsional flexibility based on adaptive pi controller with nonlinear disturbance observer. *Ocean Engineering*, 274(0):114111. https://doi.org/10.1016/j.oceaneng.2023.114111

Shi CY, Wang MZ, Yang J, et al., 2021. Performance analysis and multi-objective optimization for tubes partially filled with gradient porous media. *Applied Thermal Engineering*, 188:116530. https://doi.org/10.1016/j.applthermaleng.2020.116530

Siivonen L, Paloniitty M, Linjama M, et al., 2019. Digital valve system for iter remote handling - design and prototype testing. *Fusion Engineering and Design*, 146:1637-1641. https://doi.org/10.1016/j.fusengdes.2019.03.006

Taghizadeh A, Ghaffari A, Najafi F, 2009. Modeling and identification of a solenoid valve for pwm control applications. *Comptes Rendus Mecanique*, 337(3):131-140. https://doi.org/10.1016/j.crme.2009.03.009

Wang L, Li GX, Xu CL, et al., 2016. Effect of characteristic parameters on the magnetic properties of solenoid valve for high-pressure common rail diesel engine. *Energy Conversion and Management*, 127(0):656-666. https://doi.org/10.1016/j.enconman.2016.09.057

Wu S, Zhao XY, Li CF, et al., 2018. Multiobjective optimization of a hollow plunger type solenoid for high speed on/off valve. *IEEE Transactions on Industrial Electronics*, 65(4):3115-3124. https://doi.org/10.1109/Tie.2017.2756578

Yin HF, Sha JH, Zhou J, et al., 2023. A novel metamodel-based multi-objective optimization method using adaptive multi-regional ensemble of metamodels. *Structural and Multidisciplinary Optimization*, 66(4):1-23. https://doi.org/10.1007/s00158-023-03530-y

Youakim D, Cieslak P, Dornbush A, et al., 2020. Multirepresentation, multiheuristic a* search-based motion planning for a free-floating underwater vehicle-manipulator system in unknown environment.

Unedited

Journal of Field Robotics, 37(6):925-950. https://doi.org/10.1002/rob.21923

Yue D, Li L, Wei L, et al., 2021. Effects of pulse voltage duration on open–close dynamic characteristics of solenoid screw-in cartridge valves. *Processes*, 9(10):1722.

Zhang B, Zhong Q, Ma JE, et al., 2018. Self-correcting pwm control for dynamic performance preservation in high speed on/off valve. *Mechatronics*, 55(2018):141-150. https://doi.org/10.1016/j.mechatronics.2018.09.001

Zhang L, Dai ZY, Li T, Zhang JY, 2022. Multi-objective aerodynamic shape optimization of a streamlined high-speed train using kriging model. *Journal of Zhejiang University-SCIENCE A*, 23(3):225-242. https://doi.org/10.1631/jzus.A2100329

Zhao JH, Wang ML, Wang ZJ, et al., 2017. Different boost voltage effects on the dynamic response and energy losses of high-speed solenoid valves. *Applied Thermal Engineering*, 123(1):1494-1503. https://doi.org/10.1016/j.applthermaleng.2017.05.117

Zhao JH, Yue PF, Grekhov L, Ma XZ, 2018. Hold current effects on the power losses of high-speed solenoid valve for common-rail injector. *Applied Thermal Engineering*, 128(1):1579-1587. https://doi.org/10.1016/j.applthermaleng.2017.09.123

Zhong Q, Xu EG, Jia TW, et al., 2022. Dynamic performance and control accuracy of a novel proportional valve with a switching technology-controlled pilot stage. *Journal of Zhejiang University-SCIENCE A*, 23(4):272-285. https://doi.org/10.1631/jzus.A2100463

Zhong Q, Mao YX, Xu EG, et al., 2024. Fast dynamics and low power losses of high-speed solenoid valve based on optimized pre-excitation control algorithm. *Thermal Science and Engineering Progress*, 47:102363. https://doi.org/10.1016/j.tsep.2023.102363

Zhou C, Li JH, Duan JA, Deng GL, 2016. Control and jetting characteristics of an innovative jet valve with zoom mechanism and opening electromagnetic drive. *IEEE/ASME Transactions on Mechatronics*, 21(2):1185-1188. https://doi.org/10.1109/Tmech.2015.2482969

Electronic supplementary materials

Section S1, Table S1, Figs. S1–S2

中文概要

题　目：基于 NSGA-Ⅱ的水压高速开关阀动态响应与功率损失的协同优化

作　者： 孟令康[1]，吴德发[1]，许锋炜[2]，杨幸[1]，张铮铮[2]，刘银水[1]

机　构： [1]华中科技大学，机械科学与工程学院，中国武汉，430074；[2]中国船舶科学研究中心，中国无锡，214082；

目　的： PWM 控制参数影响高速开关阀的动态响应和功率损失。本文旨在探讨 PWM 控制参数（正向激励电压幅值、正向激励电压时间、维持电压幅值以及反向电压时间）对动态响应时间和功率损失的影响，进一步优化 PWM 控制参数，以实现高速开关阀动态响应和功率损失之间的协同优化。

创新点： 1. 通过 Maxwell 仿真，研究了 PWM 控制参数对高速开关阀动态响应和功率损失的影响；2. 通过基于代理模型的多目标优化方法，成功优化 PWM 控制参数，改善高速开关阀动态性能和功率损耗。

方　法： 1. 通过有限元仿真方法，研究了 PWM 控制参数对高速开关阀动态响应和功率损失的影响；2. 通过结合 Kriging 代理模型、NSGA-II 优化方法与 TOPSIS 决策方法，获得 PWM 控制参数最优组合解，实现高速开关阀的高动态和低功耗；3. 通过搭建高速开关阀动态实验平台，验证仿真模型、优化方法和优化结果的有效性。

结　论： 1. PWM 控制参数对高速开关阀的动态性能有显著影响。正向激励电压幅值越大，开启时间越短；负向激励电压时间越长，关闭时间越短；正向激励电压时间越长、高频维持电压幅值越大，关闭时间越长。2. PWM 控制参数显著影响高速开关阀的功率损失。随着正向激励电压幅值、正向激励电压时间、高频维持电压幅值和负向激励电压时间的增加，高速开关阀的功率损失显著增加；3. 实验和仿真数据验证了优化结果，表明所提出的优化方法能够提高高速开关阀的综合性能。实验结果与优化结果的最大偏差为 8.5%。优化后，高速开关阀的开启和关闭时间分别为 2.38 ms 和 1.29 ms，其稳态温度约为 61.5 ℃。

关键词： 协同优化；水压高速开关阀；动态响应；功率损失；PWM 控制参数

Unedited